



2

AD-A265 342



NRL/MR/6790--93-7300

Nonlinear Analysis of a Magnicon Output Cavity

B. HAFIZI

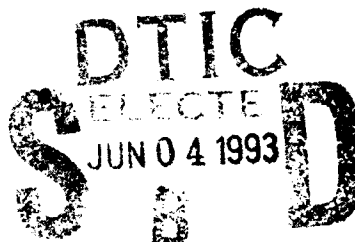
*Icarus Research
Bethesda, MD 20814*

S.H. GOLD
P. SPRANGLE

*Beam Physics Branch
Plasma Physics Division*

W.M. MANHEIMER

*Senior Scientist Fundamental Plasma Processes
Plasma Physics Division*



April 9, 1993

93-12527



Approved for public release; distribution unlimited.

93 000 036

REPORT DOCUMENTATION PAGE			Form Approved OMB No. 0704-0188	
Public reporting burden for this collection of information is estimated to average 1 hour per response, including the time for reviewing instructions, searching existing data sources, gathering and maintaining the data needed, and completing and reviewing the collection of information. Send comments regarding this burden estimate or any other aspect of this collection of information, including suggestions for reducing this burden, to Washington Headquarters Services, Directorate for Information Operations and Reports, 1215 Jefferson Davis Highway, Suite 1204, Arlington, VA 22202-4302, and to the Office of Management and Budget, Paperwork Reduction Project (0704-0188), Washington, DC 20503.				
1. AGENCY USE ONLY (Leave Blank)		2. REPORT DATE April 9, 1993		3. REPORT TYPE AND DATES COVERED Interim
4. TITLE AND SUBTITLE Nonlinear Analysis of a Magnicon Output Cavity			5. FUNDING NUMBERS JON 67-3046-03	
6. AUTHOR(S) B. Hafizi,* S.H. Gold, W.M. Manheimer, and P. Sprangle				
7. PERFORMING ORGANIZATION NAME(S) AND ADDRESS(ES) Naval Research Laboratory Washington, DC 20375-5320			8. PERFORMING ORGANIZATION REPORT NUMBER NRL/MR/6790-93-7300	
9. SPONSORING/MONITORING AGENCY NAME(S) AND ADDRESS(ES) Office of Naval Research, Arlington, VA 22217 U.S. Department of Energy, Washington, DC 20545			10. SPONSORING/MONITORING AGENCY REPORT NUMBER	
11. SUPPLEMENTARY NOTES *Icarus Research, Bethesda, MD 20814				
12a. DISTRIBUTION/AVAILABILITY STATEMENT Approved for public release; distribution unlimited.			12b. DISTRIBUTION CODE	
13. ABSTRACT (Maximum 200 words) A nonlinear analysis of the wave-particle interaction in the output cavity of a frequency-doubling magnicon amplifier is presented. The cavity is immersed in an axial magnetic field wherein electrons interact with a rotating TM_{210} mode via a gyro-resonant mechanism. The electron equations of motion and the wave equation for the radio-frequency field are derived and expressed in terms of scaled variables in order to study the general scaling of the output cavity. Single-electron, time-dependent simulation of the interaction in the cavity is performed to assess the accessibility and stability of high-efficiency states for an X-band magnicon. Results from multi-electron, steady-state simulation are presented to show the effect of spreads in electron beam radius, energy and transverse momentum on the efficiency.				
14. SUBJECT TERMS Magnicon X-Band Output cavity Efficiency Stability			15. NUMBER OF PAGES 47	
			16. PRICE CODE	
17. SECURITY CLASSIFICATION OF REPORT UNCLASSIFIED	18. SECURITY CLASSIFICATION OF THIS PAGE UNCLASSIFIED	19. SECURITY CLASSIFICATION OF ABSTRACT UNCLASSIFIED	20. LIMITATION OF ABSTRACT SAR	

CONTENTS

I. INTRODUCTION	1
II. FORMULATION	3
III. SINGLE-ELECTRON STEADY-SIMULATION; REDUCED EQUATIONS	10
IV. SINGLE-ELECTRON TIME-DEPENDENT SIMULATION; MAXWELL-LORENTZ EQUATIONS	13
V. MULTI-ELECTRON STEADY-STATE SIMULATION; LORENTZ EQUATIONS	17
VI. SUMMARY AND CONCLUSIONS	19
ACKNOWLEDGMENT	20
REFERENCES	21

DTIC QUALITY INSPECTED 2

Accession For	
NTIS GFA&I	<input checked="" type="checkbox"/>
DTIC TAB	<input type="checkbox"/>
Unannounced	<input type="checkbox"/>
Justification	
By	
Distribution/	
Availability Codes	
Dist	Avail and/or Special
A-1	

I. Introduction

The generation of the microwaves required to power future high-gradient radio-frequency (rf) accelerators will require the use of efficient and powerful sources that operate at higher frequencies than conventional S-band klystrons. Possible rf sources to meet this need include the relativistic klystron, the gyroklystron and the magnicon. In addition, there are other potential applications for such sources, including microwave power beaming. This paper presents an analysis of the electron-wave interaction in the output cavity of a magnicon. The magnicon¹⁻⁵ is an advanced version of the gyrocon⁶ and employs a scanning beam that is obtained by the passage of a magnetized pencil beam from the electron gun through a deflection system. The deflection system consists of an input cavity and one or more passive cavities, separated by drift tubes, with the entire system immersed in an axial magnetic field, B_0 . The cavities support a rotating TM_{110} mode with a frequency that is $\sim 1/2$ the gyrofrequency, $\omega_c \equiv |e|B_0/\gamma mc$. Here, e is the charge and m is the mass of an electron, γ is the relativistic factor, and c is the vacuum speed of light. The purpose of the deflection system is to spin the beam to high transverse momentum; i.e., $\alpha \equiv v_\perp/v_z > 1$. Here, v_\perp and v_z are the velocity components transverse to and along the z axis. After passing through the deflection system, the beam transverse momentum is used to drive a gyrotron-like interaction in the output cavity. The entry point of the electrons in the output cavity rotates in space about the cavity axis at the drive frequency. In the frequency-doubling version, the output cavity supports a rotating TM_{210} mode with frequency $\omega \approx \omega_c$. Each electron arrives in

the output cavity ideally gyrophased for optimum energy transfer to the rf field. Since the electrons entering the output cavity are almost completely phase-bunched and rotate in synchronism with the TM_{210} wave, the transverse efficiency may be extremely high.

At the Naval Research Laboratory (NRL) a program to develop a high-gain, second-harmonic magnicon in the X-band regime is presently under way.³ The design calls for the generation of 50 MW at 11.4 GHz and 50% efficiency, using a 200 A, 1/2 MV electron beam produced by a cold-cathode diode on the NRL Long-Pulse Accelerator Facility.⁷

This paper presents an investigation of the output cavity of a magnicon and is a follow-up of our earlier analysis of the deflection system.⁵ The equations of motion for the electrons and the wave equation for the rf field are derived. The derivation closely follows the analysis of the quasi-optical gyrotron presented in Refs. 8-10. In particular, it is assumed that the build-up of the rf field in the output cavity takes place on a time scale that is long compared to the transit time of electrons through the cavity. Scaled variables are defined and the equations are analyzed in detail to examine the efficiency of the device. Results from time-dependent and steady-state simulations of the output cavity are presented. Point design parameters for a magnicon operating in X-band are given. A major simplification in this analysis is the use of the ideal TM_{210} mode structure in the output cavity, neglecting the effects of field leakage and fringing fields in the vicinity of the beam tunnel. Additionally, the effects of space charge are neglected in the analysis.

II. Formulation

The vector potential of the electromagnetic field in the cavity is assumed to be a superposition of discrete Fourier harmonics

$$A_z(\mathbf{r}, t) = \sum_{p \neq 0} \frac{1}{i} A^{(p)} \exp(-ip\omega t) + \text{c.c.}, \quad (1)$$

where $A^{(p)}$, the amplitude of the p th Fourier component, may be decomposed in terms of the cavity modes as follows

$$A^{(p)} = \sum_{n,m,l} A_{nm,l}^{(p)}(t) J_n(p_{nm}r/a) \cos(l\pi z/L) \exp(in\phi), \quad (2)$$

where r, ϕ, z denote the cylindrical coordinates, $A_{nm,l}^{(p)}$ is a complex-valued amplitude which is a slowly-varying function of time, t , J_n is the ordinary Bessel function of the first kind of order n , p_{nm} is the m th zero of J_n , a is the radius and L is the length of the cavity and c.c. stands for complex conjugate. Figure 1 shows a cross-sectional view of the electric and magnetic field lines. The whole structure rotates azimuthally at the drive frequency, $\omega/2$. The vector potential in Eq. (1) is a solution of the wave equation in the form

$$\begin{aligned} \nabla^2 A_z - \frac{1}{c^2} \frac{\partial^2 A_z}{\partial t^2} &= \frac{4\pi I}{c} \int_{-\infty}^t dt_0 \\ &\times \int d^2 r_{\perp 0} \int d^3 p_0 f(\mathbf{r}_{\perp 0}, \mathbf{p}_0, t_0) \tilde{v}_z(\mathbf{r}_{\perp 0}, \mathbf{p}_0, t, t_0) \delta[\mathbf{r} - \tilde{\mathbf{r}}(\mathbf{r}_{\perp 0}, \mathbf{p}_0, t, t_0)], \quad (3) \end{aligned}$$

where I is the beam current and a tilde over a variable indicates that the variable is a function of t and the transverse coordinates $\mathbf{r}_{\perp 0}$ and momenta \mathbf{p}_0 at the entry

time t_0 into the cavity. The right hand side of Eq. (3) is obtained by writing the electron distribution function in the form

$$f(\mathbf{r}, \mathbf{p}, t) = \frac{I}{|e|} \int_{-\infty}^t dt_0 \times \int d^2 r_{\perp 0} \int d^3 p_0 f(\mathbf{r}_{\perp 0}, \mathbf{p}_0, t_0) \delta[\mathbf{r} - \tilde{\mathbf{r}}(\mathbf{r}_{\perp 0}, \mathbf{p}_0, t, t_0)] \delta[\mathbf{p} - \tilde{\mathbf{p}}(\mathbf{r}_{\perp 0}, \mathbf{p}_0, t, t_0)],$$

where $f(\mathbf{r}_{\perp 0}, \mathbf{p}_0, t_0)$ is the distribution function at the entrance to the cavity. The distribution function $f(\mathbf{r}, \mathbf{p}, t)$ is, by construction, a solution of the Vlasov equation.

Herein, the interest is in the excitation of the TM_{210} mode, represented by the Fourier amplitude $A_{210}^{(p)}$, with no z dependence within the cavity. Making use of the Fourier-Bessel expansion of $\delta[\mathbf{r} - \tilde{\mathbf{r}}(t, t_0)]$ and substituting Eqs. (1) and (2) into Eq. (3), one obtains

$$\sum_{p \neq 0} \exp(-ip\omega t) \left[\frac{2ip\omega}{c^2} \frac{d}{dt} + \left(\frac{p^2 \omega^2}{c^2} - k_c^2 \right) \right] \frac{A_{210}^{(p)}}{i} = \frac{4I/c}{[aJ_1(p_{21})]^2} \int_0^L \frac{dz}{L} \times \int_{-\infty}^t dt_0 \bar{v}_z \delta(z - \bar{z}) J_2(p_{21} \bar{r}/a) \exp(-2i\bar{\phi}), \quad (4)$$

where the cutoff wavenumber is defined by $k_c \equiv p_{21}/a = \omega/c$. In writing Eq. (4), the right-hand side has been simplified by assuming that there is no spread in the transverse coordinates or momenta of the electrons as they enter the cavity. The cavity radius a is determined by the boundary condition $J_2(p_{21}) = 0$. Since $p_{21} = 5.136$, the radius of the output cavity is 2.145 cm for a frequency of 11.42 GHz.

Assuming that the Fourier amplitude $A_{210}^{(p)}$ varies slowly on the time scale $2\pi/\omega$, and performing the integration $(2\pi/\omega)^{-1} \int_0^{2\pi/\omega} dt \exp(i\omega t)$ on Eq. (4), the wave

equation for $A_{210}^{(1)}$ takes the form

$$\left[\frac{2i\omega}{c^2} \frac{d}{dt} + \left(\frac{\omega^2}{c^2} - k_c^2 \right) \right] \frac{cE_0(t)}{i\omega} = \frac{4I/c}{[aJ_1(p_{21})]^2} \int_0^L \frac{dz}{L} \\ \times \int_0^{2\pi/\omega} \frac{dt_0}{2\pi/\omega} J_2\{p_{21}\tilde{r}[\tau(t_0, z), t_0]/a\} \exp\{-2i\phi[\tau(t_0, z), t_0] + i\omega\tau(t_0, z)\}, \quad (5)$$

where $E_0(t) = \omega A_{210}^{(1)}/c$ is the slowly varying complex-valued electric field amplitude and $\tau(t_0, z) = t_0 + \int_0^z dz'/v_z(t_0, z')$ is the time measured along the electron orbit. As discussed in Ref. 11, in going from Eq. (4) to Eq. (5), the order of integration has been interchanged according to the prescription $\int_0^{2\pi/\omega} dt \int_{-\infty}^t dt_0 \rightarrow \int_0^{2\pi/\omega} dt_0 \int_{-\infty}^t dt$.

Next, it is necessary to write down the equations of motion of the electrons. In terms of the independent variable z , these equations take the form

$$\frac{dv_z}{dz} = \frac{|e|\mathcal{E}_z}{\gamma mc^2} v_z - \left(\frac{|e|B_0 v_y}{\gamma mc v_z} - \frac{|e|B_y}{\gamma mc} \right), \quad (6)$$

$$\frac{dv_y}{dz} = \frac{|e|\mathcal{E}_z}{\gamma mc^2} v_y - \left(\frac{|e|B_z}{\gamma mc} - \frac{|e|B_0 v_z}{\gamma mc v_z} \right), \quad (7)$$

$$\frac{dv_z}{dz} = -\frac{|e|\mathcal{E}_z}{\gamma mc^2} \left(\frac{c^2}{v_z} - v_z \right) - \left(\frac{|e|B_y v_z}{\gamma mc v_z} - \frac{|e|B_z v_y}{\gamma mc v_z} \right), \quad (8)$$

where $\mathcal{E}_z = -(1/c)\partial A_z/\partial t$ is the rf electric field, $(B_z, B_y) = \nabla \times (A_z \mathbf{e}_z)$ is the rf magnetic field and \mathbf{e}_z is a unit vector along the z axis. Since the electrons interact with fields that are independent of the z coordinate, it follows that the canonical momentum along the z axis is conserved; i.e.,

$$P_z \equiv \gamma m v_z - \frac{|e|A_z}{c} = \text{const.} \quad (9)$$

To proceed, it is convenient to transform to guiding center variables in the guide field B_0 , defined by

$$v_x = v_\perp \cos \Phi,$$

$$v_y = v_\perp \sin \Phi,$$

$$x = X + \rho \sin \Phi,$$

$$y = Y - \rho \cos \Phi,$$

where Φ is the gyroangle, $\rho = v_\perp/\omega_c$ is the gyroradius, $\omega_c = |e|B_0/\gamma mc$ is the relativistic gyrofrequency, and (X, Y) is the guiding-center coordinate in the (x, y) -plane. The equations of motion of the guiding-center are

$$\frac{dX}{dz} = \frac{B_y}{B_0}, \quad (10)$$

$$\frac{dY}{dz} = \frac{B_x}{B_0}. \quad (11)$$

The equations of motion for the other variables may be simplified by approximating the Bessel function as follows:

$$J_2(p_{21}r/a) \exp(-2i\phi) \approx \frac{1}{2} \left(\frac{p_{21}}{2a} \right)^2 \times [R^2 \exp(-2i\Theta) - \rho^2 \exp(-2i\Phi) + 2i\rho R \exp[-i(\Phi + \Theta)]],$$

where $R \exp(i\Theta) = X + iY$ defines the guiding center radius, R , and the guiding center angle, Θ . The equations of motion of the electrons along the cavity may now be written in the form

$$\frac{\partial u_\perp}{\partial \zeta} = \frac{\epsilon}{\gamma/\gamma_0} \beta_{z0} u_\perp [\hat{R}^2 \sin \psi - 2\hat{\rho} \hat{R} \sin(\psi - \theta) + \hat{\rho}^2 \sin(\psi - 2\theta)]$$

$$+ \frac{\epsilon}{\gamma/\gamma_0} [\hat{R} \sin(\psi - \theta) - \hat{\rho} \sin(\psi - 2\theta)], \quad (12)$$

$$\begin{aligned} \frac{\partial u_z}{\partial \zeta} = & -\frac{\epsilon}{\gamma/\gamma_0} \frac{1 - \beta_{x0}^2 u_z^2}{\beta_{x0} u_z} [\hat{R}^2 \sin \psi - 2\hat{\rho} \hat{R} \sin(\psi - \theta) + \hat{\rho}^2 \sin(\psi - 2\theta)] \\ & - \frac{\epsilon}{\gamma/\gamma_0} \frac{u_\perp}{u_z} [\hat{R} \sin(\psi - \theta) - \hat{\rho} \sin(\psi - 2\theta)], \end{aligned} \quad (13)$$

$$\frac{\partial \theta}{\partial \zeta} = \frac{b_0}{\gamma/\gamma_0} \frac{1}{u_z} - \frac{\epsilon}{\gamma/\gamma_0} \frac{1}{u_\perp} [\hat{R} \cos(\psi - \theta) - \hat{\rho} \cos(\psi - 2\theta)], \quad (14)$$

where $\zeta = z/L$ is the distance along the cavity scaled to the cavity length, $\hat{R} = p_{z1}R/2a$ and $\hat{\rho} = p_{z1}\rho/2a$ are the scaled guiding-center radius and gyroradius, respectively, $u_\perp = v_\perp/v_{x0}$ and $u_z = v_z/v_{x0}$ are the components of the electron velocity scaled to the z component of the velocity at the entrance to the output cavity, v_{x0} , $\beta_{x0} = v_{x0}/c$, $b_0 = |e|B_0L/\gamma_0 m c v_{x0}$ is the scaled strength of the guide magnetic field, γ_0 is the relativistic factor at the entrance to the cavity, $E_0(t) = i|E_0(t)| \exp[i\beta(t)]$ defines the phase $\beta(t)$ of the rf field, $\epsilon = |eE_0|L/\gamma_0 m c v_{x0}$ is the scaled strength of the rf electric field and

$$\psi = (\omega L/v_{x0}) \int_0^\zeta d\zeta' / u_z(\zeta') - \beta - 2\Theta_0. \quad (15)$$

Figure 2 indicates the definition of the angle $\theta = \Phi - \Theta + \pi/2$ in terms of the guiding center angle Θ and gyroangle Φ . These angles rotate at the drive frequency $(\omega/2)$ such that at the injection point to the cavity θ does not vary with time; i.e., $\Theta(\zeta, t_0) = \Theta_0 + \omega t_0/2$, $\Phi(\zeta, t_0) = \hat{\Phi}(\zeta) + \omega t_0/2$, where Θ_0 is a constant and $\hat{\Phi}(\zeta)$ describes the variation of the gyroangle along the cavity.

When integrating the equations of motion, Eqs. (10)-(15), along the cavity, the rf field is taken to be a constant. This is a consequence of the assumption that the

temporal evolution of the rf amplitude, $E_0(t)$, takes place on a time-scale that is much longer than the electron transit time ($\approx L/v_z$) through the cavity.⁸⁻¹⁰ Hence, the use of partial derivatives in Eqs. (12)-(14).

To complete the set of governing equations, it is necessary to recast the wave equation, Eq. (5), in scaled form. We are interested in a system that is phase locked by a prebunched electron beam.¹⁰ It is assumed that the prebunched beam induces an rf field in the cavity at a frequency $\omega = ck_c + \Delta\omega$, where $\Delta\omega$ is the frequency shift with respect to the cold cavity frequency. Introducing the cavity quality factor, Q , into Eq. (5), and making use of the small argument expansion of the Bessel function, the wave equation reduces to

$$\left(\frac{\partial}{\partial\tau} + \frac{1}{2}\right)\epsilon = \hat{I} \int_0^1 d\zeta \left[\hat{R}^2 \sin\psi - 2\hat{\rho}\hat{R} \sin(\psi - \theta) + \hat{\rho}^2 \sin(\psi - 2\theta) \right], \quad (16)$$

$$\epsilon \left(\Delta\hat{\omega} - \frac{\partial\beta}{\partial\tau} \right) = \hat{I} \int_0^1 d\zeta \left[\hat{R}^2 \cos\psi - 2\hat{\rho}\hat{R} \cos(\psi - \theta) + \hat{\rho}^2 \cos(\psi - 2\theta) \right], \quad (17)$$

where $\hat{I} = IQL / \{I_A k_c [aJ_1(p_{21})]^2\}$ is the scaled beam current, $I_A = (mc^3/|e|)\gamma_0\beta_{z0}$ is the Alfvén current, $\tau = ck_c t / Q$ is the scaled time and $\Delta\hat{\omega} = Q\Delta\omega / ck_c$ is the scaled frequency mismatch. It is important to note that the integration over the entry time t_0 in Eq. (5) can be trivially performed and does not appear in Eqs. (16) and (17). This is due to the special nature of the magnicon, in which electrons enter the output cavity prebunched, and also due to our assumption that there is no spread in the initial transverse coordinates or momenta. Thus, to study the complete evolution of the system, it is only necessary to study the passage of a single electron through the cavity. This is the basis of the simulation results presented in Secs. III and IV. We shall address the issue of non-ideal beam effects in Secs. V.

The efficiency is defined as $\eta = (\gamma_0 - \gamma_f)/(\gamma_0 - 1)$, where γ_f is the relativistic factor at the cavity exit. Making use of Eqs. (12), (13) and (16), it follows that, in steady state,

$$\eta = \frac{\beta_{z0}\gamma_0}{2(\gamma_0 - 1)} \frac{\epsilon^2}{\bar{I}}. \quad (18)$$

It should be remarked that the expression in Eq. (18) is simply a restatement of the balance between the power extracted from the electron beam and the power dissipated in the finite- Q output cavity.

In studying the efficiency of conversion of electron energy into rf energy as an electron traverses the output cavity, it is useful to define the detuning, Δ , that measures the deviation of the gyrofrequency from the rf frequency:

$$\Delta \equiv \frac{(\omega/c)L}{\beta_{z0}} - b_0. \quad (19)$$

In common with the gyrotron, for zero detuning the efficiency should be small and significant conversion will be achieved only for positive detuning.¹² An estimate for the optimum detuning may be obtained by choosing the magnitude of the guide field so as to maintain gyroresonance on the average, assuming that the electrons are brought to a complete rest at the end of the interaction. That is, $B_0^{opt} = (mc\omega/|e|)(\gamma_0 + 1)/2$. Making use of Eq. (19), the optimum detuning, Δ^{opt} , is given by

$$\Delta^{opt} = \frac{(\omega/c)L}{\beta_{z0}} \frac{\gamma_0 - 1}{2\gamma_0}, \quad (20)$$

III. Single-Electron Steady-State Simulation; Reduced Equations

The purpose of this section is to present steady-state simulation results obtained from numerical solution of the reduced equations derived in the previous section. Neglecting guiding-center drifts, Eqs. (12)-(17), with $\partial/\partial\tau$ set equal to zero, constitute a simplified set of equations that can be solved to rapidly scan the parameter space. Since these equations are expressed in scaled form, the simulation results may be used to obtain point designs for a variety of physical systems.

Equations (10) and (11) represent the drift of the electron guiding-center. The right-hand sides of Eqs. (10) and (11) are on the order of 10 % or less for the examples described in detail here. This, along with the close agreement between steady-state simulation results based on the reduced equations, and those based on the full Lorentz equations in Sec. IV, justifies the neglect of guiding-center drifts.

All the simulation results in this paper assume that on entering the output cavity, the guiding center of an electron is located off the cavity axis at a distance equal to the gyroradius. This assumption is roughly borne out by our previous investigation of the electron beam as it is spun up in the deflection cavities.⁵

The input parameters for the simulation are the beam energy at injection, the scaled cavity length, $k_e L$, and the detuning, Δ . Equation (20) is used to obtain an order-of-magnitude estimate for the detuning that leads to high efficiency. The angle θ , which is defined following Eq. (15) and in Fig. 2, is related to the gyroangle and the guiding-center angle at the entrance to the cavity. This angle is also an

input parameter, being determined in part by the length of the drift tube leading to the output cavity. For a given value of the scaled electric field, ϵ , the scaled current, \hat{I} , and the efficiency are determined from Eqs. (16) and (18), respectively. The plots presented in this section are obtained by scanning over all rf phase values, $-\pi \leq \beta < \pi$, to determine the *maximum* efficiency and the corresponding values of the scaled frequency shift, the scaled current, and the rf phase. To leading order, the approximation $\omega \approx ck_c$ is employed in Eq. (15) and the frequency shift is then simply obtained from Eq. (17). The last input parameter is the initial beam α . Two examples will be discussed in detail, corresponding to the initial values $\alpha = 1$ and $\alpha = 1.5$.

Case (i) : $\alpha = 1$

Figure 3 shows the results of the single-particle, steady-state simulation of the reduced equations for $\alpha = 1$. The parameters for this simulation are listed in Table I, the three different detunings corresponding to the three curves in each plot. Figures 3(a), (b), (c), and (d) show the efficiency, η , the scaled current, \hat{I} , the scaled frequency shift, $\Delta\hat{\omega}$, and ψ_0 , respectively. The latter is the value of the phase angle ψ at the entrance to the cavity. From Eq. (15), it follows that $\psi_0 = -\beta - 2\Theta_0$, thus relating Fig. 3(d) to the rf phase, β . The abscissa in each plot is the scaled electric field.

On examining Fig. 3, it is interesting to note that significant conversion efficiency ($> 50\%$) may be obtained with a beam α as small as 1. It is also interesting to note the discontinuity in some of the curves at high values of scaled electric field.

This discontinuity results from a new local efficiency maximum (as a function of phase) becoming the global maximum. (Our plots of *maximum* efficiency as a function of electric field do not reveal the variation of the efficiency with rf phase; see Ref. 10.)

It should be noted that the existence of steady-state solutions does not guarantee their accessibility or their stability in an experiment that must grow from rf noise. In order to investigate the accessibility of the high-efficiency solutions that the scanning code locates, we will make use of a time-dependent code, as discussed in Sec. IV.

Case (ii) : $\alpha = 1.5$

Figure 4 shows the results of the single-particle, steady-state simulation of the reduced equations for $\alpha = 1.5$. The parameters for this simulation are listed in Table II, the three different detunings corresponding to the three curves in each plot. Figures 4(a), (b), (c) and (d) show the efficiency, η , the scaled current, \hat{I} , the scaled frequency shift, $\Delta\hat{\omega}$, and ψ_0 , respectively. The general behavior of the plots is similar to that in Fig. 3, although no discontinuity is apparent in this case. Note that, as expected, the efficiency can be quite high, reaching up to 70 % for the case with $\Delta = 5.788$.

IV. Single-Electron Time-Dependent Simulation; Maxwell-Lorentz Equations

In Sec. III we presented a panoramic view of the magnicon output cavity based on the highly simplified equations derived in Sec. II. Figures 3 and 4 permit one to design an output cavity by translating the scaled variables according to the constraints of any particular experiment.

It is pointed out in Sec. III that the maximum efficiency steady-state predicted by a time-independent code may not be accessible or stable in an experiment in which the fields build up from noise. To address this issue one can employ a time-dependent code to determine which one of the optimum-efficiency final states indicated in Figs. 3 and 4 are true steady states of the system. The time-dependent simulation results presented here are obtained from the full set of Maxwell-Lorentz equations, Eqs. (5)-(8), following the motion of a single electron through the cavity and studying the build-up of the rf field over a much longer time scale.

The parameters for the time-dependent simulation are chosen by locating a high efficiency point on the solid curve in Fig. 3 or Fig. 4, and reading off the corresponding value for the scaled current, and the frequency shift. An important criterion in choosing an operating point is to minimize the electric field, consistent with an acceptable efficiency, in order to avoid breakdown problems. In the examples considered in this paper, the maximum tolerable electric field is taken to be ≈ 300 kV/cm. A further constraint on the parameters relates to the length of the cavity. Conservation of canonical momentum, Eq. (9), implies that the kinetic z -

momentum, $p_z \equiv \gamma m v_z$, can vary along the cavity. We find that there is an optimal cavity length for which the efficiency is a maximum and p_z is a minimum as the electron exits the cavity. This point will be clarified presently. The current I to be used in the time-dependent code is determined by taking a reasonable value for the cavity quality factor, Q (≤ 1000). The choice for the cavity length and the detuning determine the value of the guide field through Eq. (19). Having chosen the parameters, the time-dependent code is used to search for the maximum efficiency by fine-tuning the frequency shift around the value determined from Fig. 3(c) or Fig. 4(c). It must be emphasized that the time-dependent simulation results are based on the full, unapproximated set of Maxwell-Lorentz equations and may therefore differ to some extent from those based on the reduced equations of motion.

Case (i): $\alpha = 1$

Table III lists the parameters for the time-dependent simulation of the case with initial beam $\alpha = 1$, $\Delta = 3.776$ and $\hat{I} = 6.5$. Figures 5(a), (b), and (c) show plots of the electric field amplitude, the rf phase, and the efficiency as functions of time. Figure 5 shows that the system settles into a steady state after a transient that lasts ≈ 60 ns. Figure 5(a) shows that the electric field builds up to about 305 kV/cm, Fig. 5(b) shows that the phase settles to an asymptotic value 1.1 rad, and Fig. 5(c) shows the final efficiency in this field is about 52 %.

Figures 6 (a), (b), and (c) show plots of the axial momentum (normalized to its initial value), efficiency, and α for an electron traversing the output cavity in the final steady-state field. The modulation of the electron momentum, p_z , is seen

to be correlated with the modulation on the efficiency curve. The scale-length for the modulation is $\approx 2\pi\beta_z/k_c$. The length of the cavity has been chosen to be 4.75 cm so that, on exiting the cavity, p_z is a minimum, and therefore the efficiency is a maximum. In this sense, it appears that there is an optimal length for the output cavity, which may be fine tuned to obtain the maximum efficiency. Figure 6(c) shows that the value of α declines as the electron spins down on traversing the cavity.

In terms of the scaled variables, the final state of the time-dependent code is compared with the corresponding point on Fig. 3 in Table IV. This table shows close agreement between the results from the steady-state simulation (labeled SSS) of reduced equations and the time-dependent simulation (labeled TDS) of the full Maxwell-Lorentz equations.

It must be pointed out that the steady-state simulations are deficient in a very important respect. Namely, the questions of accessibility and stability of the predicted final states of the cavity, shown in Fig. 3, remain unresolved. As a case in point, we compare in Table V the results of the time-dependent and steady-state codes at the point at which the scaled current $\bar{I} = 17.13$ and the detuning $\Delta = 4.776$, which lies at the extreme right of Fig. 3 on the dotted curve, and ostensibly corresponds to the highest efficiency. Examination of Table V, however, reveals that for this point the time-dependent code asymptotes to a final state with a much smaller efficiency. This example highlights the fact that not all of the optimum-efficiency states in Fig. 3, or Fig. 4, are accessible and stable final states of the rf field that

is built up from noise in the output cavity.

Case (ii): $\alpha = 1.5$

Table VI lists the parameters for the time-dependent simulation of the case with initial beam $\alpha = 1.5$, $\Delta = 4.788$ and $\hat{I} = 6.75$. Figures 7(a), (b) and (c) show plots of the electric field amplitude, the rf phase and the efficiency as functions of time. This figure shows that the system settles into a steady state after a transient that lasts ≈ 25 ns. Figure 7(a) shows that the electric field builds up to about 230 kV/cm, Fig. 7(b) shows that the phase settles to an asymptotic value -1.2 rad, and Fig. 7(c) shows the final efficiency in this field is about 63 %.

Figures 8(a), (b) and (c) show plots of the axial momentum (normalized to its initial value), efficiency, and α for an electron traversing the output cavity in the final steady-state field. The length of the cavity has been chosen to be 6.2 cm so that p_z is a minimum at the end of the cavity and therefore the efficiency is a maximum. Figure 8(c) shows that the electron spins down on traversing cavity, although not to the same extent as that in Case (i).

In terms of the scaled variables, the final state of the time-dependent code is compared with the corresponding point on Fig. 4 in Table VII. Examination of Table VII shows close agreement between the results from the steady-state simulation of reduced equations and the time-dependent simulation of the full Maxwell-Lorentz equations. A comparison has also been made between the simulations for $\hat{I} = 10.9$ on the solid curve in Fig. 4; close agreement between the results is obtained.

V. Multi-Electron Steady-State Simulation; Lorentz Equations

On the basis of the single-electron simulation of the preceding sections, point designs for operation of a magnicon output cavity, with $\alpha = 1$ or $\alpha = 1.5$, have been obtained. The purpose of this section is to assess the role of beam quality, as measured by spreads in the input parameters of the beam, on the efficiency. The numerical results presented in this section are obtained by solving the Lorentz equations of motion for a collection of electrons that represent spreads in the initial values of α , the guiding center radius, R , or γ . In all cases, the electron distribution is taken to be a "top-hat", with initially uniform loading of the electrons. This suffices to give an order-of-magnitude estimate of the effect of beam quality on the efficiency.

The parameters for the multi-electron, steady-state simulation are listed in Tables III and VI. The asymptotic rf phase obtained from the time-dependent simulation is used as an input parameter to the steady-state code. The electron equations of motion are integrated along the cavity for several field amplitudes to pin-point the rf steady-state that is in power balance with the given electron current. In the figures, the spreads are given in terms of the root-mean-square (rms) deviation from the mean of the corresponding quantity. The abscissa in the figures represent the ratio of the rms to the mean value, expressed as a percentage.

Before proceeding, it is important to remark on a basic premise of the steady-state simulation results of this section. As the spread in a beam parameter increases from zero, the rf field at which power balance is obtained varies. For a sufficiently

large value of the spread, however, there is, in some cases, a sudden jump in the rf field amplitude required for power balance. In the figures to be described, the maximum value of the spread is limited to lie below the point at which the sudden jump takes place. Nevertheless, it cannot be guaranteed that a multi-electron, *time-dependent* code would lead to results identical to those presented here.

Case (i): $\alpha = 1$

Figures 9 (a), (b), and (c) show the decline in the efficiency due to increasing spreads in α , guiding center radius, R , and γ , respectively. The rapid decrease of efficiency with energy spread is specially noteworthy. Obviously this implies that the design of the deflection system must be particularly cognizant of this sensitive dependence on energy spread.

Case (ii): $\alpha = 1.5$

Figures 10 (a), (b), and (c) show the decline in the efficiency due to increasing spreads in α , guiding center radius, R , and γ , respectively. Once again, one finds that the optimum efficiency is extremely sensitive to a spread in γ . Additionally, comparison of Figs. 9 and 10 shows that the beam with the higher α is relatively more sensitive to spreads in the beam parameters.

VI. Summary and Conclusions

The electron-wave interaction in the output cavity of a frequency-doubling, magnetic-field-immersed magnicon has been analyzed in a series of simulation studies. In this presentation the output cavity is considered as an entity that is separate from the deflection system, with the electron beam parameters corresponding to what is expected on the basis of our earlier studies of the deflection system.⁵

Single-electron, steady-state simulation of reduced equations of motion were used to rapidly scan the parameter space and locate a desirable operating point. A single-electron, time-dependent code was then employed to ensure that the chosen final state was an accessible and stable operating point of an amplifier wherein the rf grew from noise. Finally, a multi-electron, steady-state code was used to study the sensitivity of the point design to spreads in the beam parameters.

In conclusion, it is useful to recall the salient points of this work. First, as indicated in Figs. 6 and 8, for an ideal beam, it is possible to choose the cavity length so as to convert not only the transverse momentum but also part of the axial momentum into rf field energy. Second, based on the runs made with the time-dependent code, we have found that some of the final states determined by the steady-state code are accessible and stable, and some are not. Third, an efficient ($> 50\%$) final state with $\alpha = 1$ is achievable. Finally, the efficiency of the output cavity is most sensitive to energy spread on the beam.

Acknowledgment

This work was supported by the Division of High Energy Physics, Office of Energy Research, U. S. Department of Energy under Interagency Agreement No. DE-AI05-91ER-40638 and by the U. S. Office of Naval Research. The computer time used in this work was supported in part by a Naval Research Laboratory Cray X-MP 6.1 Production Run Grant.

References

- [1] M. M. Karliner, E. V. Kozyrev, I. G. Makarov, O. A. Nezhevenko, G. N. Ostreiko, B. Z. Persov and G. V. Serdobintsev, "The Magnicon—An Advanced Version of the Gyrocon," *Nucl. Instrum. Methods Phys. Res.*, vol. A269, pp. 459-473, 1988.
- [2] O. Nezhevenko, "The Magnicon: A New rf Power Source for Accelerators," in *Proc. IEEE Particle Accel. Conf.*, 1991, edited by L. Lizama and J. Chen (IEEE, New York, 1991), pp. 2933-2942.
- [3] S. H. Gold, B. Hafizi, W. M. Manheimer and C. A. Sullivan, "Design of a High-Perveance, Field-Immersed Magnicon," in *Conf. Digest—Sixteenth Int. Conf. Infrared and Millimeter Waves*, SPIE-vol. 1576, edited by M. R. Siegrist, M. Q. Tran and T. M. Tran (Centre de Recherches en Physique des Plasmas, École Polytechnique Fédérale de Lausanne, Lausanne, Switzerland, 1991), pp. 4-5; S. H. Gold, C. A. Sullivan, B. Hafizi and W. M. Manheimer, "Study of Gain in C-Band Deflection Cavities for a Frequency-Doubling Magnicon," submitted to *IEEE Trans. Plasma Sci.*, 1993.
- [4] W. M. Manheimer, "Theory and Conceptual Design of a High-Power Highly Efficient Magnicon at 10 and 20 GHz," *IEEE Trans. Plasma Sci.*, vol. PS-18, pp. 632-645, 1990.
- [5] B. Hafizi, Y. Seo, S. H. Gold, W. M. Manheimer and P. Sprangle, "Analysis

- of the Deflection System for a Magnetic-Field-Immersed Magnicon Amplifier," *IEEE Trans. Plasma Sci.*, vol. PS-20, pp. 232-239, 1992.
- [6] G. I. Budker, M. M. Karliner, I. G. Makarov, S. N. Morosov, O. A. Nezhevenko, G. N. Ostreiko and I. A. Shekhtman, "The Gyrocon—An Efficient Relativistic High-Power VHF Generator," *Part. Accel.*, vol. 10, pp. 41-59, 1979.
- [7] N. C. Jaitly, M. Coleman, S. Eckhouse, A. Ramrus, S. H. Gold, R. B. McCowan and C. A. Sullivan, "1 MV Long Pulse Generator with Low Ripple and Low Droop," in *Digest of Technical Papers - Eighth IEEE International Pulsed Power Conf.*, edited by K. Prestwich and R. White (IEEE, New York, 1991), pp. 161-165.
- [8] A. Bondeson, W. M. Manheimer and E. Ott, "Multimode Analysis of Quasi-Optical Gyrotrons and Gyroklystrons," in *Infrared and Millimeter Waves*, K. Button, Ed., New York: Academic 1983, vol. 9, pp. 309-340.
- [9] T. M. Antonsen, B. Levush and W. M. Manheimer, "Stable Single Mode Operation of a Quasioptical Gyrotron," *Phys. Fluids B*, vol. 2, pp. 419-426, 1990.
- [10] W. M. Manheimer, B. Levush and T. M. Antonsen, "Equilibrium and Stability of Free-Running, Phase-Locked and Mode-Locked Quasi-Optical Gyrotrons," *IEEE Trans. Plasma Sci.*, vol. PS-18, pp. 350-368, 1990.
- [11] P. Sprangle, C. M. Tang and W. M. Manheimer, "Nonlinear Theory of Free Electron Lasers and Efficiency Enhancement," *Phys. Rev. A*, vol. 21, pp. 302-319, 1980.

- [12] V. L. Bratman, N. S. Ginzburg, G. S. Nusinovich, M. I. Petelin and P. S. Strelkov, "Relativistic Gyrotrons and Cyclotron Autoresonance Masers," *Int. J. Electronics*, vol. 51, pp. 541-567, 1981.

Table captions

Table I: Parameters for steady-state simulation of a magnicon amplifier output cavity for three detunings. Initial beam $\alpha = 1$.

Table II: Parameters for steady-state simulation of a magnicon amplifier output cavity for three detunings. Initial beam $\alpha = 1.5$.

Table III: Parameters for time-dependent simulation of an X-band magnicon amplifier output cavity. Initial beam $\alpha = 1$.

Table IV: Comparison of single-particle time-dependent simulation (TDS) and single-particle steady-state simulation (SSS) of reduced equations. Beam $\alpha = 1$, detuning $\Delta = 3.776$ and scaled current $\hat{I} = 6.5$.

Table V: Comparison of single-particle time-dependent simulation (TDS) and single-particle steady-state simulation (SSS) of reduced equations. Beam $\alpha = 1$, detuning $\Delta = 4.776$ and scaled current $\hat{I} = 17.13$.

Table VI: Parameters for time-dependent simulation of an X-band magnicon amplifier output cavity. Initial beam $\alpha = 1.5$

Table VII: Comparison of single-particle time-dependent simulation (TDS) and single-particle steady-state simulation (SSS) of reduced equations. Beam $\alpha = 1.5$, detuning $\Delta = 4.788$ and scaled current $\hat{I} = 6.75$.

Table I

Voltage	500	kV
$k_c L$	11.37	cm
Beam α	1	
Detuning Δ_1	2.776	
Detuning Δ_2	3.776	
Detuning Δ_3	4.776	
θ	$\pi/2$	

Table II

Voltage	500 kV
$k_c L$	14.85 cm
Beam α	1.5
Detuning Δ_1	3.788
Detuning Δ_2	4.788
Detuning Δ_3	5.788
θ	π

Table III

Frequency	11.43	GHz
Voltage	500	kV
Current I	180.1	A
Cavity Radius	2.145	cm
Cavity Length	4.75	cm
Cavity Quality Factor Q	200	
Beam α	1	
Magnetic Field B_0	6.455	kG
Detuning Δ	3.776	
Gyroangle Φ	0	
Guiding Center Radius R	3.2	mm
Frequency Shift $\Delta\omega/2\pi$	6	MHz

Table IV

	TDS	SSS
ϵ	2.34	2.28
$\Delta\hat{\omega}$	0.11	0.12
$-\beta$	-1.1	-0.9
η	51.9 %	48.4 %

Table V

	TDS	SSS
ϵ	0.7	4
$\Delta\hat{\omega}$	0.475	0.475
$-\beta$	2.9	-1.7
η	1.8 %	57.6 %

Table VI

Frequency	11.4138	GHz
Voltage	500	kV
Current I	172	A
Cavity Radius	2.145	cm
Cavity Length	6.2	cm
Cavity Quality Factor Q	130	
Beam α	1.5	
Magnetic Field B_0	6.85	kG
Detuning Δ	4.788	
Gyroangle Φ	$\pi/2$	
Guiding Center Radius R	3.5	mm
Frequency Shift $\Delta\omega/2\pi$	-10.2	MHz

Table VII

	TDS	SSS
ϵ	2.95	2.9
$\Delta\hat{\omega}$	-0.12	-0.12
$-\beta$	1.2	1.2
η	63 %	60.6 %

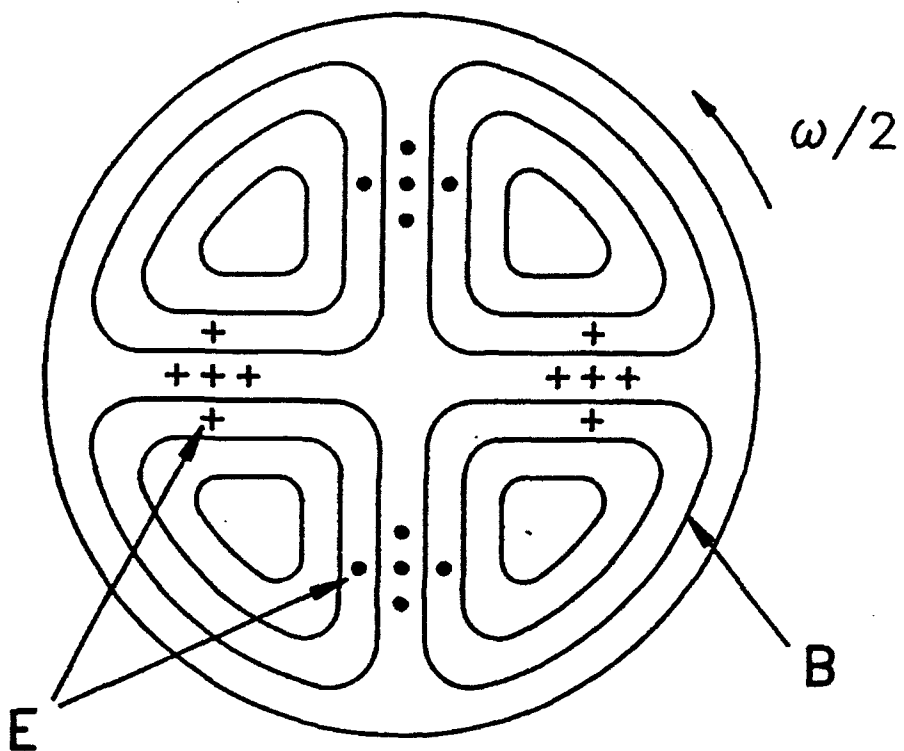


Figure 1: TM_{210} mode pattern in magnicon output cavity. Mode pattern rotates azimuthally at drive frequency, $\omega/2$. Electric field is shown by “+” and “•” and magnetic field is indicated by solid curves.

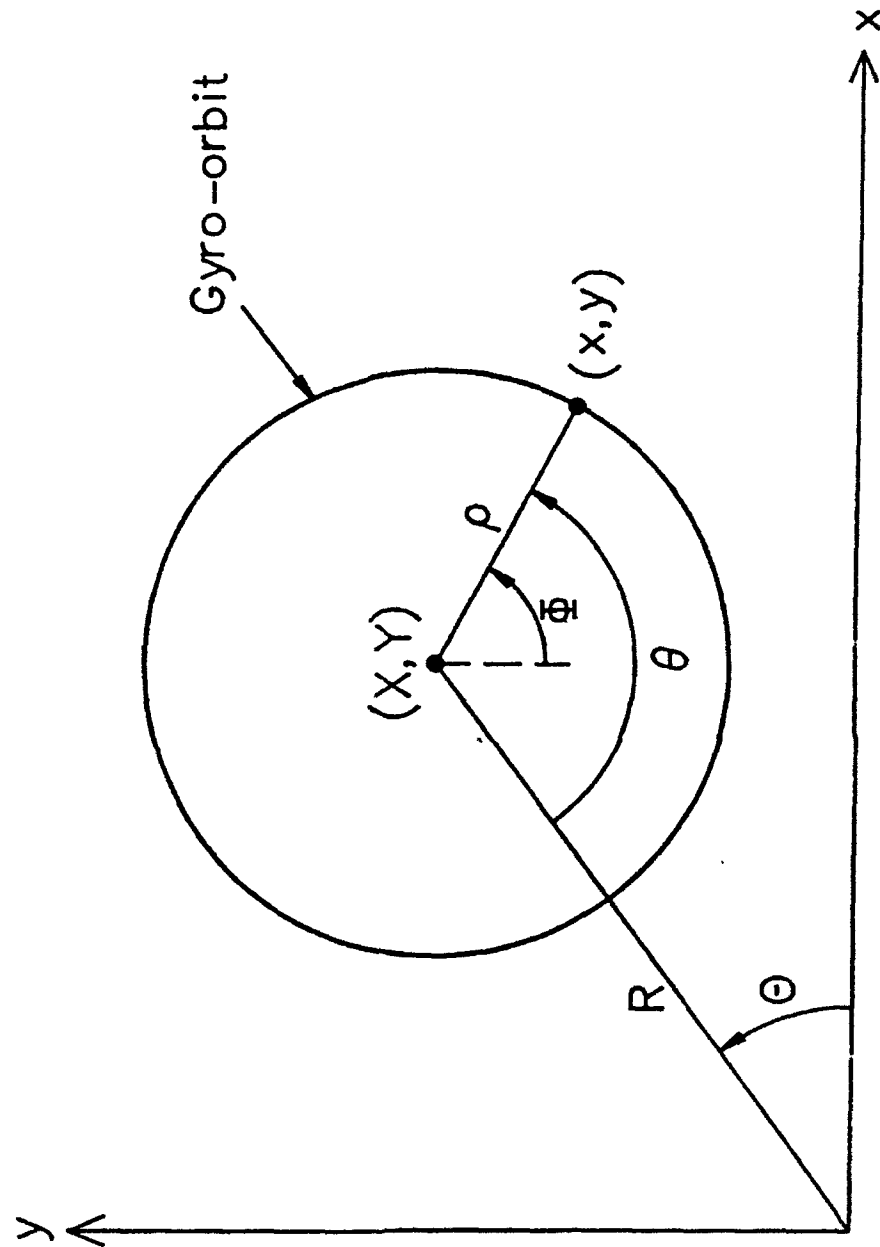


Figure 2: Projection of gyro-orbit onto transverse plane. Electron is at (x, y) and guiding center is at (X, Y) . (R, Θ) denotes guiding center radius and angle, and (ρ, Φ) denotes gyroradius and gyroangle. Angle $\theta = \Phi - \Theta + \pi/2$ is fixed for electrons entering output cavity.

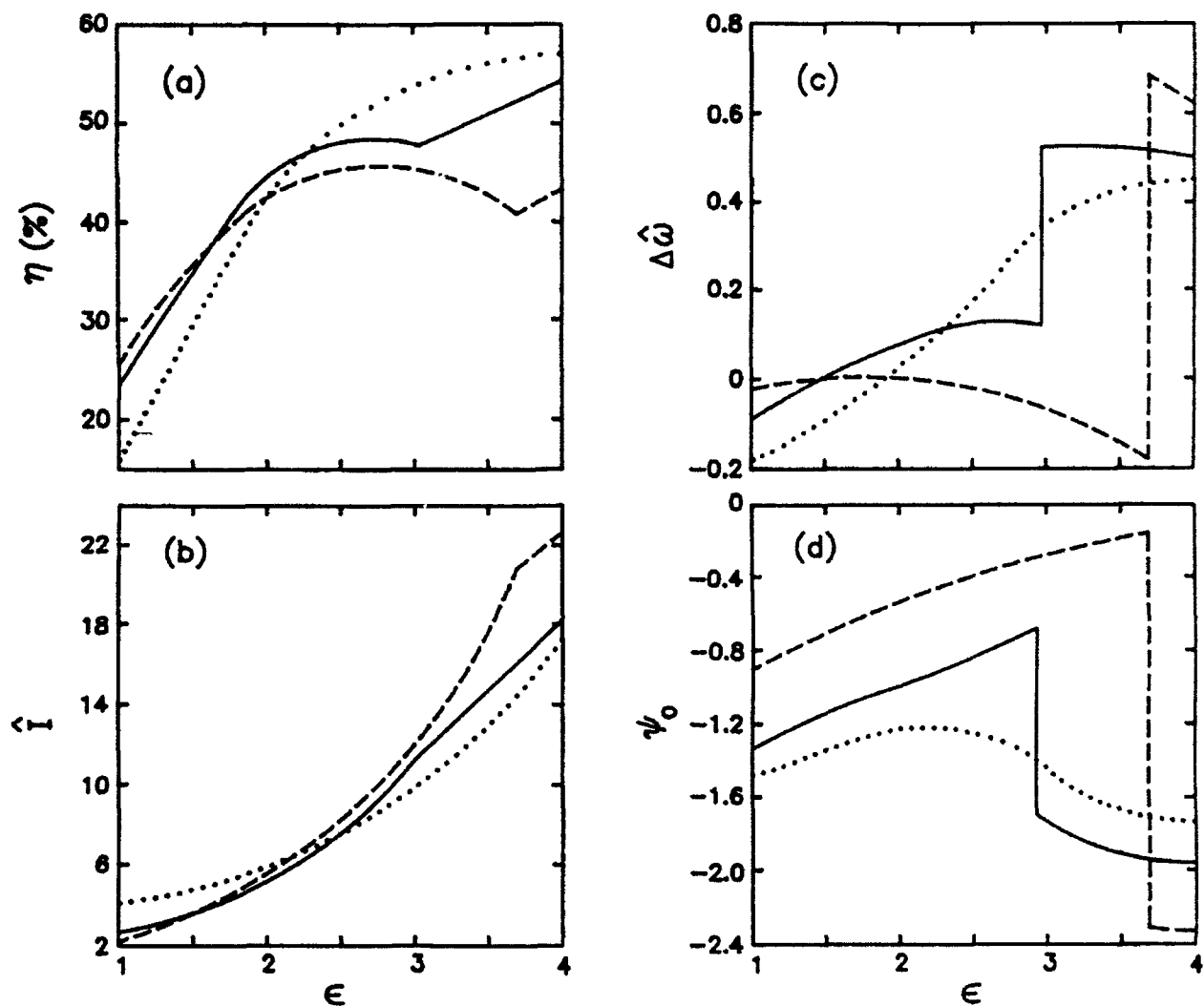


Figure 3: Results from single-electron, steady-state simulation of reduced equations for initial beam $\alpha = 1$ and three detunings, $\Delta_1 = 2.776$ (- - -), $\Delta_2 = 3.776$ (—), $\Delta_3 = 4.776$ (.....). (a) Efficiency, η ; (b) Scaled current, \hat{I} ; (c) Scaled frequency shift, $\Delta\hat{\omega}$; (d) ψ_0 . Abscissa is scaled electric field, ϵ .

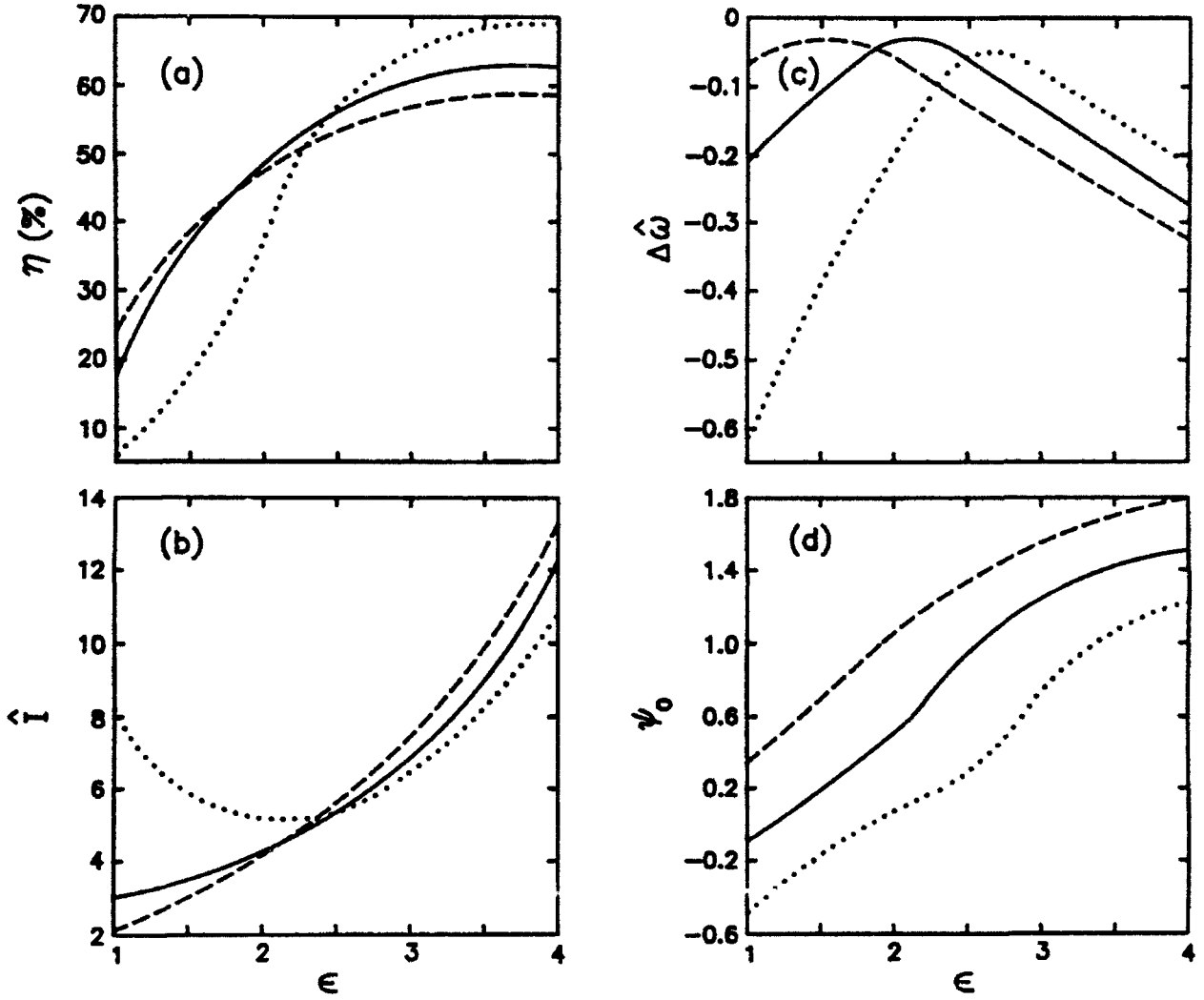


Figure 4: Results from single-electron, steady-state simulation of reduced equations for initial beam $\alpha = 1.5$ and three detunings, $\Delta_1 = 3.788$ (- - -), $\Delta_2 = 4.788$ (—), $\Delta_3 = 5.788$ (.....). (a) Efficiency, η ; (b) Scaled current, \hat{I} ; (c) Scaled frequency shift, $\Delta\hat{\omega}$; (d) ψ_0 . Abscissa is scaled electric field, ϵ .

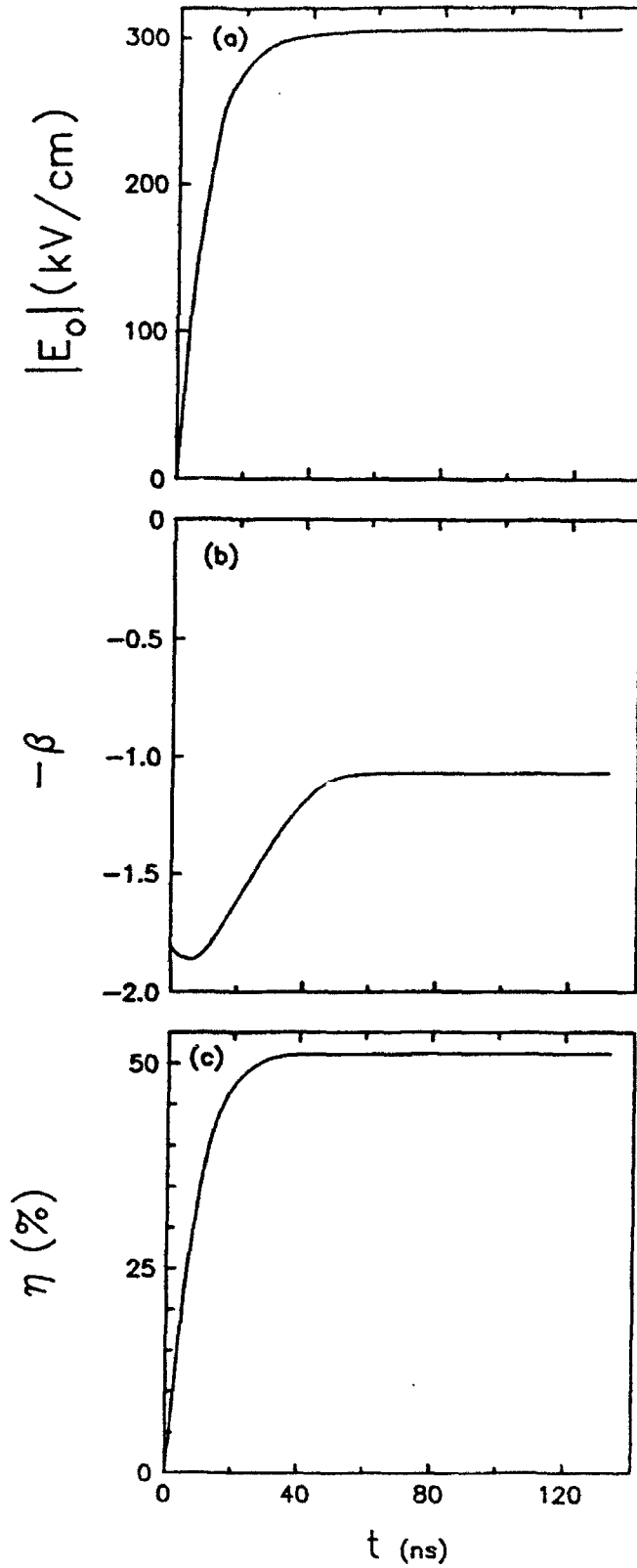


Figure 5: Results from single-electron, time-dependent simulation of X-band magnicon with initial beam $\alpha = 1$ and detuning $\Delta = 3.776$. (a) Electric field amplitude, $|E_0|$; (b) RF phase, $-\beta$; (c) Efficiency, η . Abscissa is time.

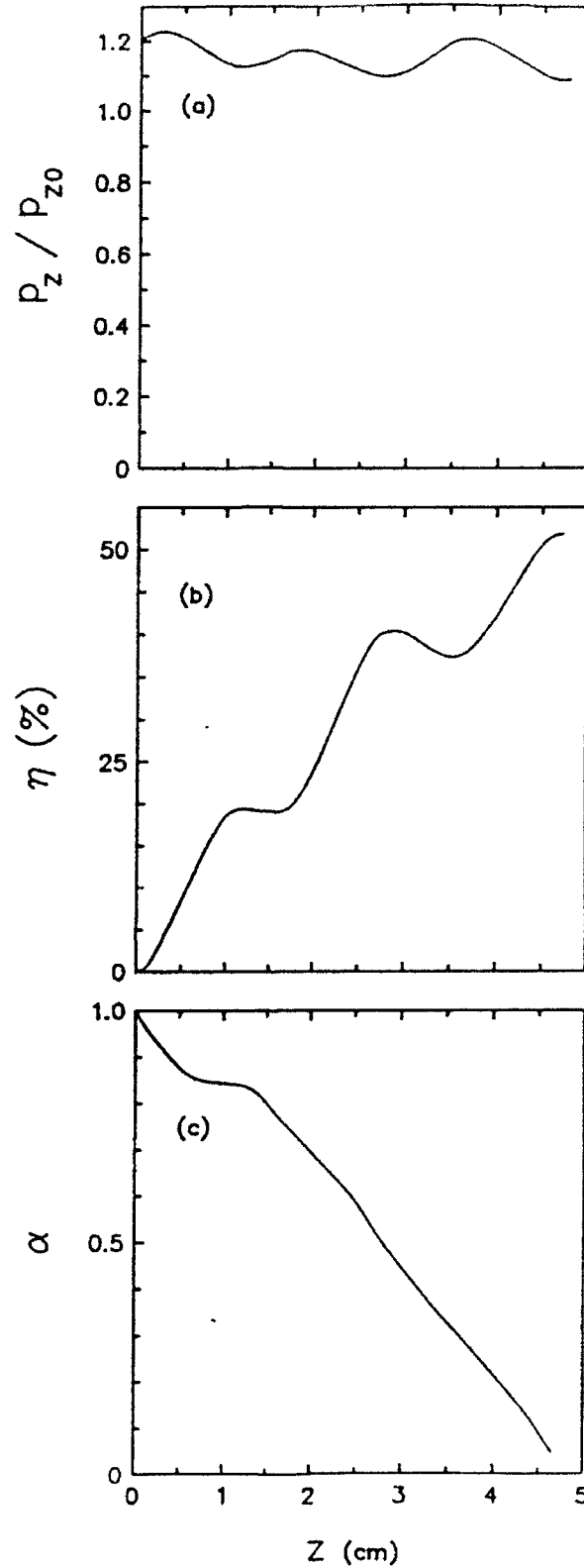


Figure 6: Results from single-electron, time-dependent simulation of X-band magnicon with initial beam $\alpha = 1$ and detuning $\Delta = 3.776$. (a) Axial kinetic momentum normalized to initial value, p_z/p_{z0} ; (b) Efficiency, η ; (c) α . Abscissa is distance along cavity. These plots correspond to motion of an electron through cavity in final steady state.

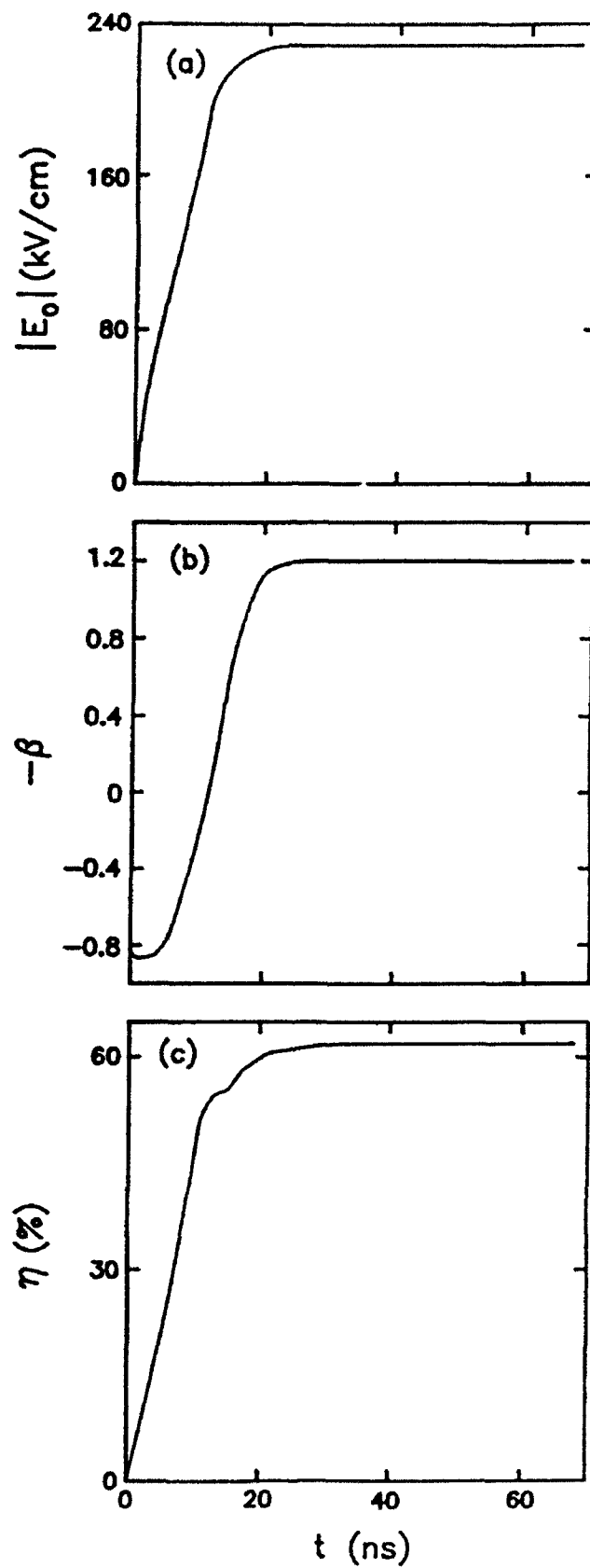


Figure 7: Results from single-electron, time-dependent simulation of X-band magnicon with initial beam $\alpha = 1.5$ and detuning $\Delta = 4.788$. (a) Electric field amplitude, $|E_0|$; (b) RF phase, $-\beta$; (c) Efficiency, η . Abscissa is time.

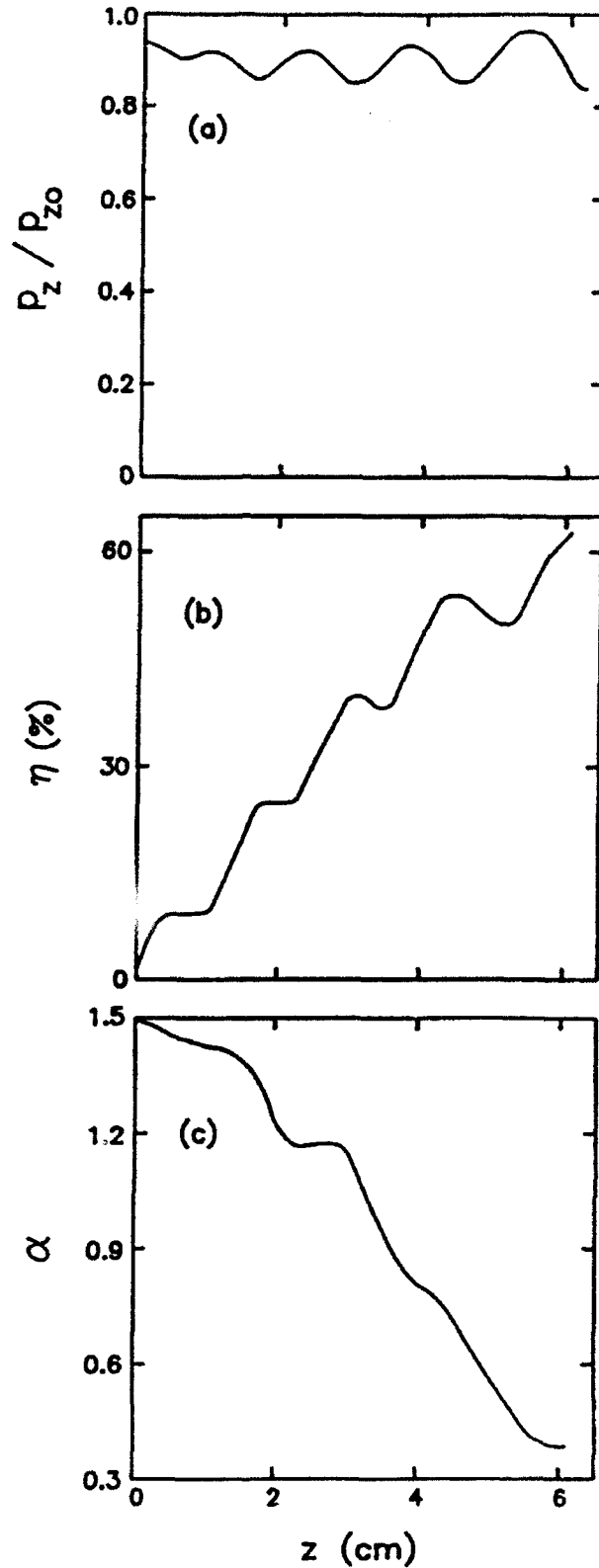


Figure 8: Results from single-electron, time-dependent simulation of X-band magnicon with initial beam $\alpha = 1.5$ and detuning $\Delta = 4.788$. (a) Axial kinetic momentum normalized to initial value, p_z/p_{z0} ; (b) Efficiency, η ; (c) α . Abscissa is distance along cavity. These plots correspond to motion of an electron through cavity in final steady state.

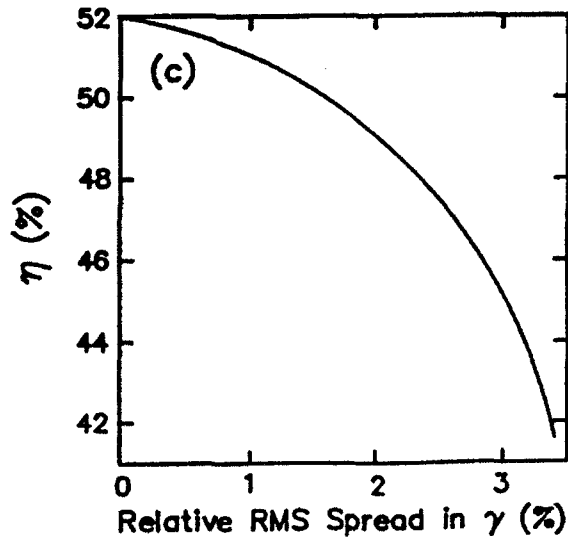
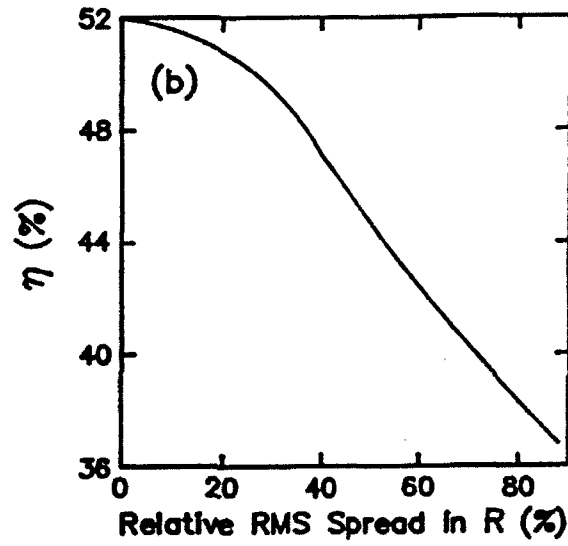
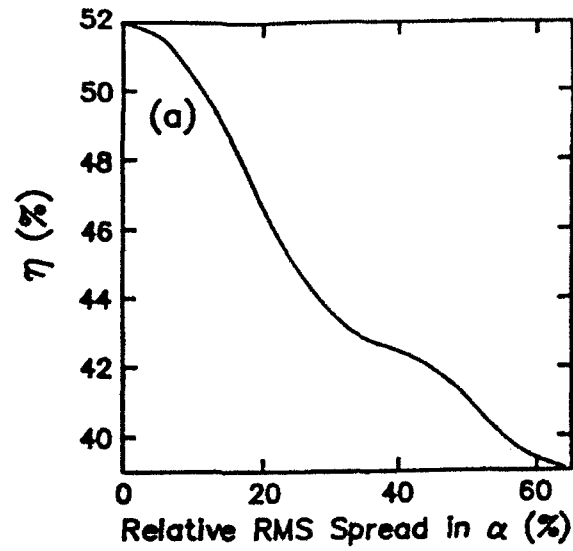


Figure 9: Results from multi-electron, steady-state simulation with initial beam $\alpha = 1$.

Efficiency versus relative rms deviations : (a) $\langle (\alpha - \langle \alpha \rangle)^2 \rangle^{1/2} / \langle \alpha \rangle$,
 (b) $\langle (R - \langle R \rangle)^2 \rangle^{1/2} / \langle R \rangle$, (c) $\langle (\gamma - \langle \gamma \rangle)^2 \rangle^{1/2} / \langle \gamma \rangle$. Here,
 $\langle \rangle$ indicates an average over electron distribution.

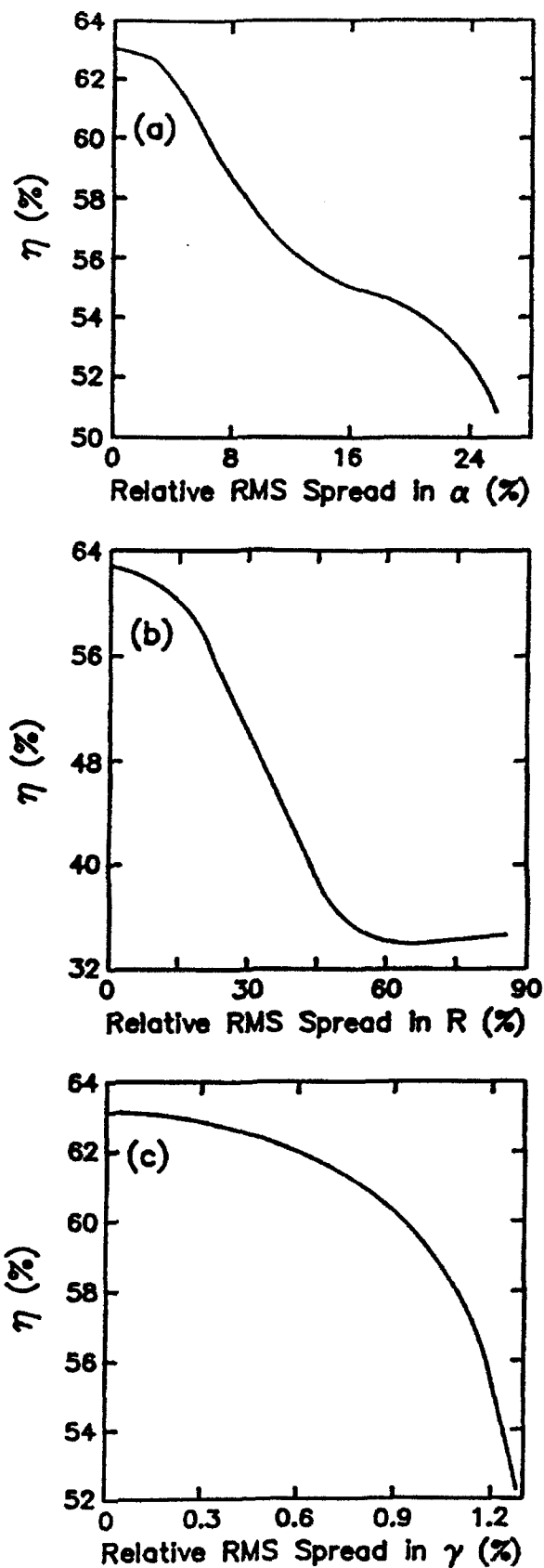


Figure 10: Results from multi-electron, steady-state simulation with initial beam $\alpha = 1.5$.

Efficiency versus relative rms deviations : (a) $\langle (\alpha - \langle \alpha \rangle)^2 \rangle^{1/2} / \langle \alpha \rangle$,
 (b) $\langle (R - \langle R \rangle)^2 \rangle^{1/2} / \langle R \rangle$, (c) $\langle (\gamma - \langle \gamma \rangle)^2 \rangle^{1/2} / \langle \gamma \rangle$. Here,
 $\langle \rangle$ indicates an average over electron distribution.